AGU100 ADVANCING EARTH AND SPACE SCIENCE

Geophysical Research Letters

RESEARCH LETTER
10.1029/2018GL080171

Special Section:
The Arctic: An AGU Joint Special Collection

The Ice-Ocean Governor: Ice-Ocean Stress Feedback Limits Beaufort Gyre Spin-Up

Gianluca Meneghello[1], John Marshall[1], Jean-Michel Campin[1], Edward Doddridge[1], and Mary-Louise Timmermans[2]

[1]Department of Earth, Atmospheric and Planetary Sciences, Massachusetts Institute of Technology, Cambridge, MA, USA, [2]Department of Geology and Geophysics, Yale University, New Haven, CT, USA

Key Points:
- Spin-up of the Beaufort Gyre is regulated by a negative feedback between ice-ocean stress and surface currents: an ice-ocean stress governor
- In the present Arctic system, the governor is likely a key process controlling the equilibration of the gyre
- Continued sea ice loss will likely lead to reduced effectiveness of the governor and change the fundamental internal dynamics of the gyre

Supporting Information:
- Supporting Information S1

Correspondence to:
G. Meneghello,
gianluca.meneghello@gmail.com

Citation:
Meneghello, G., Marshall, J. C., Campin, J.-M., Doddridge, E., & Timmermans, M.-L. (2018). The ice-ocean governor: Ice-ocean stress feedback limits Beaufort Gyre spin-up, *Geophysical Research Letters*, *45*. https://doi.org/10.1029/2018GL080171

Received 23 AUG 2018
Accepted 29 SEP 2018
Accepted article online 17 OCT 2018

©2018. American Geophysical Union. All Rights Reserved.

Abstract The Beaufort Gyre is a key circulation system of the Arctic Ocean and its main reservoir of freshwater. Freshwater storage and release affects Arctic sea ice cover, as well as North Atlantic and global climate. We describe a mechanism that is fundamental to the dynamics of the gyre, namely, the *ice-ocean stress governor*. Wind blows over the ice, and the ice drags the ocean. But as the gyre spins up, currents catch the ice up and turn off the surface stress. This governor sets the basic properties of the gyre, such as its depth, freshwater content, and strength. Analytical and numerical modeling is employed to contrast the equilibration processes in an ice-covered versus ice-free gyre. We argue that as the Arctic warms, reduced sea ice extent and more mobile ice will result in a deeper and faster Beaufort Gyre, accumulating more freshwater that will be released by Ekman upwelling or baroclinic instability.

Plain Language Summary The Beaufort Gyre, located north of Alaska and Canada, is a key circulation system of the Arctic Ocean. Changes in its depth and circulation influence the evolution of the Arctic sea ice cover, the North Atlantic circulation, and the global climate. The gyre is driven by persistent, ice-mediated winds, accumulating surface freshwater toward the center, deepening the gyre, and spinning up its currents. We describe a mechanism, dubbed here the *ice-ocean governor*, in which the interaction of surface currents with the ice regulates the depth of the Beaufort Gyre: The spinning up of the gyre reduces the relative speed between the ocean and the ice, and hence the freshwater accumulation. This competes with, and we argue is more important than, the release of freshwater by flow instability, which moves water from the center toward the periphery. In the current climate the depth and speed of the Beaufort Gyre are mainly set by the governor, but this may change in a warming world where reduced ice cover will render the ice-ocean governor less effective. The resulting deeper, swifter gyre will likely exhibit more variability in its freshwater storage and flow speeds.

1. Introduction

Anticyclonic winds centered over the Arctic Ocean's Beaufort Gyre (BG) force a lateral Ekman transport bringing surface freshwater toward the center of the gyre and steepening isopycnals. This convergence increases the freshwater content of the BG and spins up its geostrophic current (McPhee et al., 2009; Proshutinsky et al., 2002, 2015; Proshutinsky & Johnson, 1997; Proshutinsky et al., 2009; Timmermans et al., 2011; Zhang et al., 2016). Freshwater accumulation, storage, and release from the BG, controlled by these wind-driven dynamics, have far-reaching influence on Arctic and global climate (Proshutinsky et al., 2015). However, wind variability alone cannot explain the variability in freshwater content (Giles et al., 2012). Gyre spin-up and freshwater increase, proportional to the curl of the ocean surface stress, are complicated by the presence of sea ice cover, which acts to decouple wind and surface ocean stresses through internal lateral stresses and interacts with surface currents. Here we present a theoretical framework that illustrates how the interaction between under-ice geostrophic ocean currents and sea ice cover (described by the observational studies of Dewey et al., 2018; Kwok & Morison, 2017; Meneghello et al., 2017, 2018; Zhong et al., 2018) plays a key role in equilibrating the freshwater content of the BG. Inspired by self-limiting speed regulators (or governors) in mechanical systems (Bennet, 1993; Maxwell, 1867), we call this mechanism the *ice-ocean stress governor*. More specifically, the term *governor* refers to a mechanism for regulating the speed of a system by automatically restricting the flow of water, air, fuel, etc., when the speed increases and increasing the flow when it decreases (Murray et al., 2018).

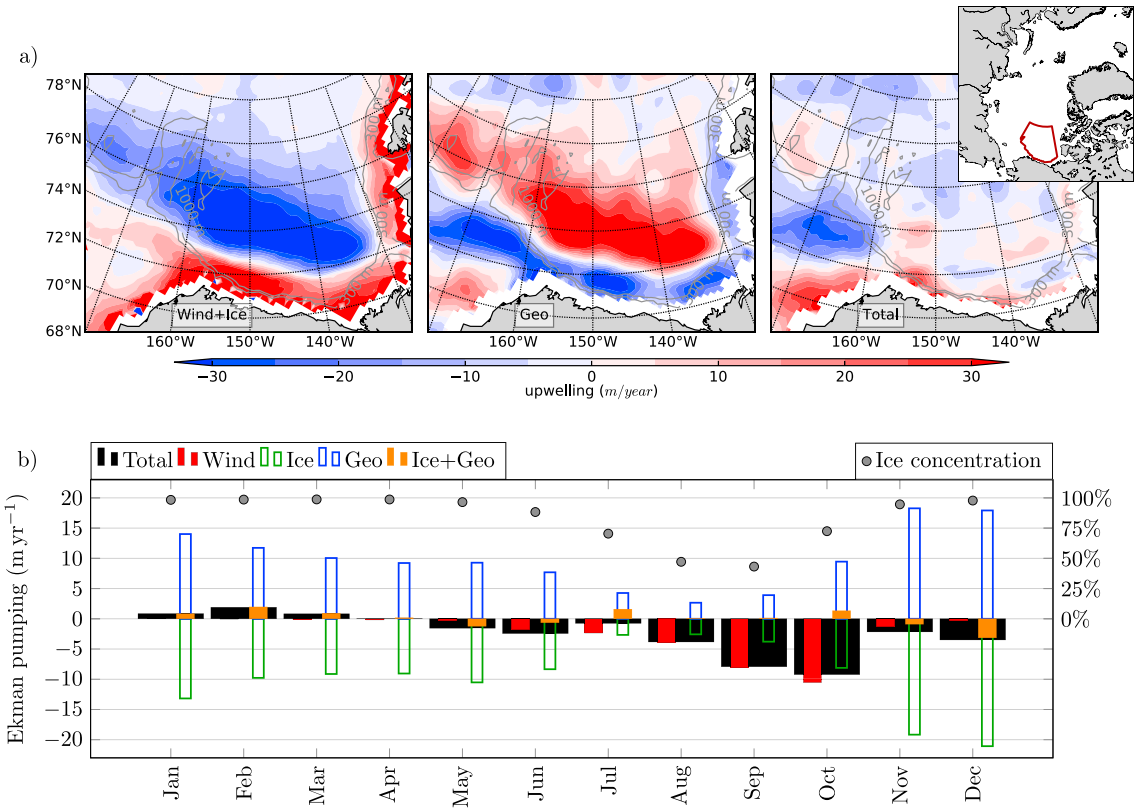

Figure 1. Ekman pumping climatology. (a) Mean Ekman pumping over 2003–2014; negative (blue) indicates downwelling and positive (red) upwelling. (left) Downwelling estimates locally exceed 30 m/year if the geostrophic current is neglected; (middle) inclusion of the geostrophic current results in an upwelling effect, largely compensating the ice-driven downwelling; (right) the net Ekman pumping, the sum of the previous two panels, yields moderate downwelling together with patches of upwelling. The Beaufort Gyre Region is marked by a red line in the inset. (b) Monthly Ekman pumping climatology integrated over the Beaufort Gyre Region and its partitioned contributions, where negative indicates downwelling. Black bars show total Ekman pumping, equivalent to the right panel in (a). Red and orange bars show pumping induced by winds over ice-free regions and by ice in ice-covered regions, respectively. Within ice-covered regions, downward pointing empty green bars show downwelling induced by the ice if the geostrophic current is neglected, while the upward directed blue bars show upwelling induced by the geostrophic currents flowing under the sea ice. Blue and green bars largely balance each other and exactly balance if $\boldsymbol{u}_{\text{rel}} = 0$. Gray dots represent ice concentration. All data and methods are described in Meneghello et al. (2018).

The total stress $\boldsymbol{\tau}$ at the ocean surface is a combination of ice-ocean stress $\boldsymbol{\tau}_i$ and air-ocean stress $\boldsymbol{\tau}_a$, each of which may be estimated by a quadratic drag law, weighted by the sea ice concentration α:

$$\boldsymbol{\tau} = \alpha \underbrace{\rho C_{Di} \left|\boldsymbol{u}_{\text{rel}}\right| \left(\boldsymbol{u}_{\text{rel}}\right)}_{\boldsymbol{\tau}_i} + (1-\alpha) \underbrace{\rho_a C_{Da} \left|\boldsymbol{u}_a\right| \left(\boldsymbol{u}_a\right)}_{\boldsymbol{\tau}_a}. \tag{1}$$

$C_{Di} = 0.0055$ and $C_{Da} = 0.00125$ are dimensionless drag coefficients for the ice-ocean and air-ocean stress respectively, $\rho = 1{,}028$ kg/m^3 is water density, and $\rho_a = 1.25$ kg/m^3 is air density. In the computation of $\boldsymbol{\tau}_a$, the surface ocean velocity, of a few centimeters per second, is considered negligible with respect to a wind velocity $\boldsymbol{u}_a$ of a few meters per second. However, surface ocean velocity cannot be neglected in the estimation of $\boldsymbol{\tau}_i$: The ice-ocean relative velocity $\boldsymbol{u}_{\text{rel}}$ is expressed as the difference between the ice velocity $\boldsymbol{u}_i$ and the geostrophic surface ocean velocity $\boldsymbol{u}_g$. That is, $\boldsymbol{u}_{\text{rel}} = (\boldsymbol{u}_i - \boldsymbol{u}_g)e^{i\beta}$, where β is a turning angle taking into account the Ekman layer.

Figure 1, modified from Meneghello et al. (2018), shows how the intensity of the ocean surface currents plays a central role in modulating the Ekman pumping in an ice-covered gyre (Dewey et al., 2018; Meneghello et al., 2017, 2018; Zhong et al., 2018). Estimates of wind- and ice-induced downwelling can exceed 30 m/year locally if the geostrophic current is neglected (Figure 1a, blue region in the left panel; see also Yang, 2006, 2009). However, this is largely compensated by the upwelling effect of the surface current flowing below the ice (red region in the central panel), acting as a negative feedback and reducing the downwelling. That is, the governor drives the system toward $\boldsymbol{u}_{\text{rel}} = 0$. Consequently, the net Ekman downwelling is strongly reduced

(right panel). A monthly climatology of the 2003–2014 Ekman pumping and its components averaged over the Beaufort Gyre Region (Figure 1b) shows how the total Ekman pumping is reduced by the geostrophic current and even reversed during the months of January, February, and March (Meneghello et al., 2018).

Through analytical calculations and an idealized numerical model, we demonstrate here how the governor acts as a mechanism to equilibrate the freshwater content of the gyre. For example, should the anticyclonic ice-ocean stress curl —and freshwater accumulation rate—intensify, the geostrophic flow of the gyre will strengthen, reducing the surface stress until the governor turns off the ice-ocean stress. This is a distinct alternative to the eddy equilibration mechanism first proposed for the Southern Ocean (Karsten et al., 2002; Marshall & Radko, 2003) and more recently extended to the BG (Davis et al., 2014; Lique et al., 2015; Manucharyan & Spall, 2016; Manucharyan et al., 2016; Meneghello et al., 2017; Yang et al., 2016).

To explore the governor mechanism and test our theoretical model, we analyze the response of an idealized gyre under two different limit-case scenarios: (i) an ice-driven gyre ($\alpha = 1$ in equation (1), in which forcing depends purely on gradients of $\boldsymbol{\tau} = \boldsymbol{\tau}_i$) and (ii) an ice-free, wind-driven gyre ($\alpha = 0$, in which forcing depends purely on gradients of $\boldsymbol{\tau} = \boldsymbol{\tau}_a$). We conclude with a discussion of the implications of the governor for the Arctic Ocean's circulation and its freshwater content.

2. The Ice-Ocean Stress Governor

We run numerical experiments employing a high-resolution idealized model of the BG based on the Massachusetts Institute of Technology General Circulation Model (MITgcm) (Marshall, Adcroft, et al., 1997; Marshall, Hill, et al., 1997) and designed to capture both mesoscale eddy processes and the ice-ocean stress governor mechanism (for numerical details see the supporting information). The results are then compared with a simple analytical model that captures the essential mechanism of the ice-ocean stress governor. Our focus is on the equilibrium response of the gyre and how it is approached in time. All simulations begin with a uniformly stratified, flat-bottomed ocean at rest. The ocean is spun up via a steady axisymmetric, anticyclonic, wind/ice field with zero speed at the center of the domain and reaching a maximum at a radius of 300 km (see the supporting information), broadly consistent with observations (Meneghello et al., 2018). Surface freshwater is pumped down through the action of these wind-/ice-driven surface stresses and a parameterized bottom Ekman layer is used to dissipate momentum. Parameters are chosen to efficiently damp bottom currents on a time scale of a few months. For the ice-driven gyre, imposing the ice velocity (rather than, e.g., estimating it based on wind speed) represents the limiting case in which lateral internal ice stresses effectively decouple ice and wind fields. Wind and ice velocity magnitudes are chosen to induce the same surface stress $\boldsymbol{\tau}_0$ and Ekman pumping w_{Ek} when the ocean is at rest and are broadly consistent with observations. The stress, and hence the freshwater accumulation rate, remains constant in the ice-free case $\alpha = 0$ but evolves and, in fact, diminishes in time in the ice-driven case $\alpha = 1$ as the surface currents spin up to match the ice speed. Five experiments are run for each scenario, varying ice and wind velocities; we diagnose the gyre response by computing the maximum sea surface height (SSH) anomaly η and maximum depth anomaly of the $S = 31$ isohaline h and discuss the associated change in freshwater content (see the supporting information) stored in the gyre (Figure 2).

2.1. Ice-Driven Gyre ($\alpha = 1$): Stress Equilibrated

We begin by describing the evolution of a typical ice-covered simulation in which the governor operates (Figure 2a, left panels, and Figure 2b, thick blue line). Ice-covered experiments impose anticyclonic ice drift with a range of maximum speeds broadly in agreement with observations (Meneghello et al., 2018); our example simulation has an ice speed maximum of 8 cm/s, corresponding to a surface stress $\tau_0 = 0.04$ N/m^2. Initially, the ocean is at rest and the applied surface stress gives rise to an Ekman pumping of order $w_{\mathrm{Ek}} \approx \tau_0/(\rho f R) \approx$ 30 m/year, where $R \approx 300$ km is the radius of the gyre and $f = 1.45 \times 10^{-4}$ s^{-1}. As time progresses, surface freshwater is accumulated toward the center of the gyre, giving rise to a central SSH maximum and steepening isohaline surfaces (Figure 2a, left panels), and a geostrophic current is spun up; by year 10, the ocean surface speed is almost equal to the ice drift speed (Figure 2a, top row). Around year 20, h stabilizes at a depth of around 60 m, and the freshwater content anomaly equilibrates at a maximum of around 20,000 km^3 (Figure 2b, thick blue line). Weak baroclinic instability develops around year 26, but the ice-ocean stress governor is sufficiently efficient in the ice-covered scenario that baroclinic instability does not play any appreciable role in gyre equilibration. Baroclinic eddies are likely additionally damped by the relaxation of the surface velocity

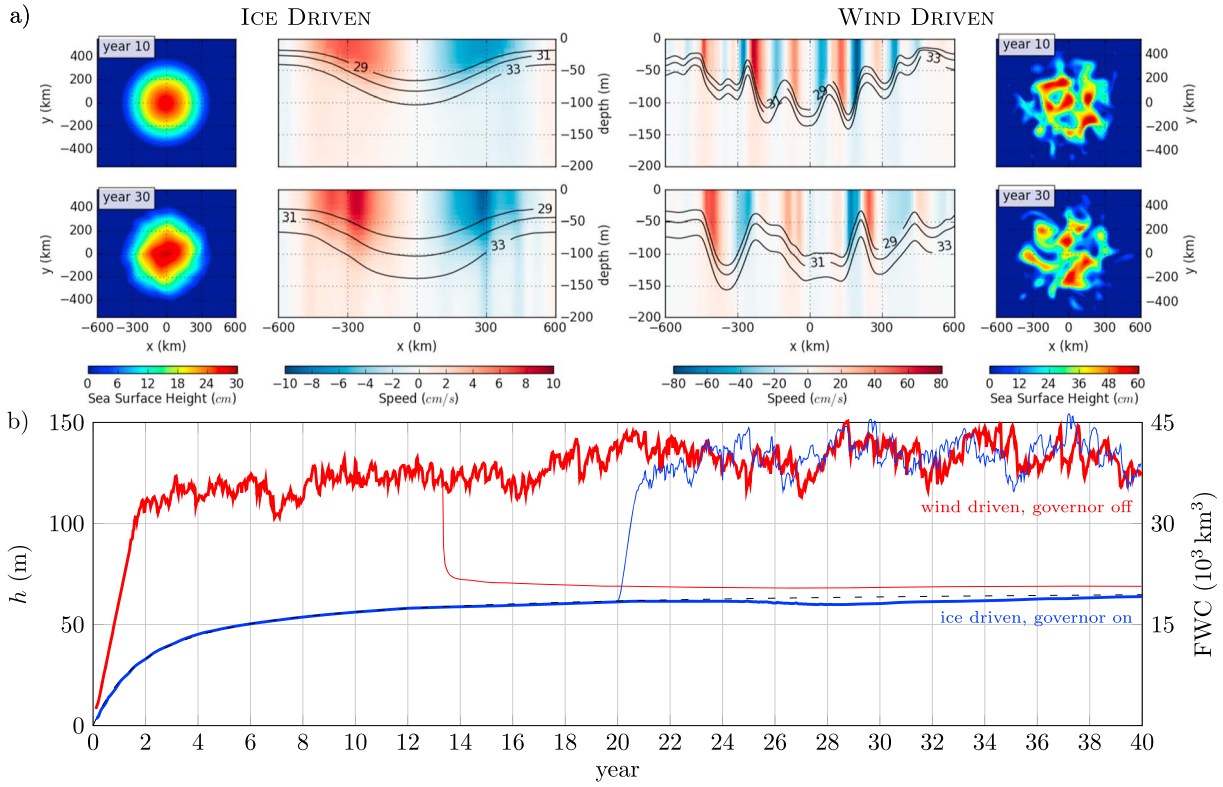

Figure 2. (a) Instantaneous sea surface height (exterior panels), vertical section of salinity (middle panels, black contours) and speed (middle panels, color) at years 10 (top row) and 30 (bottom row) for the ice-driven ($\alpha = 1$ and $u_i = 8$ cm/s, left) and the wind-driven ($\alpha = 0$ and $u_a = 4.8$ m/s, right) scenarios. Note the different ranges (color scales) between the two cases. Only the top 200 m of the 800-m domain depth are shown in the central panels. (b) Depth anomaly h of the $S = 31$ isohaline and equivalent freshwater content anomaly (FWC, right axis), for the ice-driven $\alpha = 1$ (blue) and wind-driven $\alpha = 0$ (red) scenarios. For $\alpha = 1$, Ekman pumping spins up the gyre until the surface ocean speed approaches the ice drift speed such that $\boldsymbol{u}_{\text{rel}}$, and the ice-ocean stress, approaches 0. The dashed black line is a fit of equation (6) and is indistinguishable from the numerical solution before year 20. Evidence of very weak baroclinic instability is visible in the later stages of the evolution (around year 26). For $\alpha = 0$, the gyre inflates at a constant rate proportional to the Ekman pumping until it reaches a quasi-equilibrium in which Ekman pumping is balanced by baroclinic instability and lateral eddy fluxes out of the gyre. The thin lines in panel (b) show the transition between an ice-covered and an ice-free state (blue), and vice versa (red).

to the ice velocity. We note that the time at which baroclinic instability develops depends on the gyre depth and, ultimately, on the magnitude of the imposed ice velocity.

To develop a conceptual model, we assume that the isopycnal depth anomaly h increases at a rate proportional to w_{Ek}, which in the ice-driven case is proportional to the curl of the surface stress $\boldsymbol{\tau}_i$ and thus depends on the geostrophic velocity $\boldsymbol{u}_g$ via equation (1). We may then write

$$\frac{\mathrm{d}h}{\mathrm{d}t} = \frac{\gamma}{\rho f}\frac{\tau_i}{R}, \tag{2}$$

where γ is a dimensionless constant that depends on the spatial distribution of the Ekman pumping and the geometry of the isopycnal lens.

In order to obtain an analytical solution that enables us to identify controlling parameters, we suppose the bottom current to be small so that the magnitude of the surface geostrophic velocity may be estimated by the thermal wind relationship as follows:

$$u_g \sim \frac{g'}{f}\frac{h}{R}, \tag{3}$$

where $g' = g\Delta\rho/\rho$ is the reduced gravity, $\Delta\rho$ is the vertical density difference between the top and bottom of the model domain, and $\Delta\rho/\rho \approx 0.0063$. This assumption is consistent with observations—see Figure 4 of Meneghello et al. (2017)—and the strong damping of the barotropic mode in our numerical model. It limits, however, our analysis to time scales longer than baroclinic adjustment time scales; these are the time scales of interest for the gyre equilibration. The close agreement between theory and simulation, reported below, attests to the validity of these approximations.

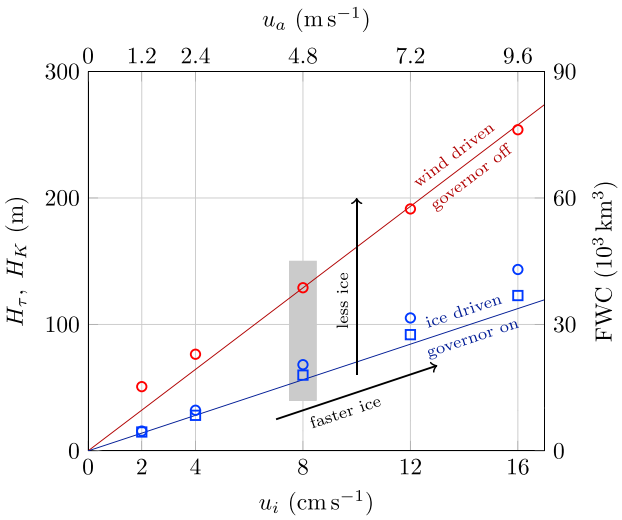

Figure 3. Asymptotic depth anomaly H and equivalent freshwater content anomaly (FWC, right axis, see the supporting information for details), for five different model runs of the wind-driven (H_K, red circles) and ice-driven (H_τ, blue circles) scenarios, as a function of the wind (u_a) and ice (u_i) velocity, respectively. Lines show the theoretical prediction from equation (5) for the ice-driven (blue) scenario with R = 300 km and $g' = 0.0063g$, and the least squares fit for the wind-driven (red) scenario. Blue squares represent the isopycnal depth anomaly computed from the model sea surface height anomaly as $\frac{g}{g'}\eta$. The gray area marks the example cases plotted in Figure 2. Arrows indicate two possible mechanisms, which result in changes in the depth and freshwater content of the wind-driven gyre: an increase in the speed of the imposed ice drift and a reduction in ice cover making the governor less effective at limiting the ice-ocean stress.

Using equations (3) and (1), equation (2) may be expressed as

$$\frac{dh}{dt} = \frac{H_\tau}{T_\tau}\left(1 - \frac{h}{H_\tau}\right)^2, \tag{4}$$

where

$$H_\tau = \frac{f}{g'}Ru_i \quad \text{and} \quad T_\tau = \frac{(fR)^2}{\gamma g' C_{Di} u_i} \tag{5}$$

are ice stress-equilibrated length and time scales, respectively, and we have assumed $h < H_\tau$(equivalent to $u_g < u_i$) to remove the absolute value from equation (1). The length scale H_τ is the stress-equilibrated steady state isopycnal depth (i.e., $dh/dt = 0$ when $h = H_\tau$) and is proportional to the ice velocity u_i and inversely proportional to the stratification g'. It can be seen from equations (3) and (5) that $h = H_\tau$ is equivalent to $u_g = u_i$ (i.e., $u_{\text{rel}} = 0$ in (1)). In this limit the gyre has been equilibrated by the ice-ocean stress governor. Equation (4), with initial condition $h(t = 0) = 0$, then has solution

$$h = H_\tau\left(\frac{t}{t + T_\tau}\right). \tag{6}$$

Values of H_τ and T_τ can be obtained by fitting equation (6) to the diagnosed isopycnal depth anomaly from each simulation. The fitted curve, shown by a black dashed line in Figure 2, is almost indistinguishable from the numerical results until the development of baroclinic instability around year 26.

The fitted H_τ and T_τ are plotted as a function of the ice velocity with blue circles in Figures 3 and 4. Blue lines in the same figures show the model prediction according to (5) with R = 300 km, $g' = 0.0063g$, $C_{Di} = 0.0055$, and $\gamma = 1.75$: Clearly, the model does a very good job at capturing both the isopycnal depth anomaly and the time scale. This is even more true when the isopycnal depth anomaly is computed from the model SSH anomaly as $\frac{g}{g'}\eta$ (blue squares); the difference between blue squares and blue circles quantifies the departure of the numerical model from the zero bottom flow assumption.

2.2. Wind-Driven Gyre ($\alpha = 0$): Eddy Equilibrated

The reference wind-driven experiment (Figure 2a, right, and Figure 2b, thick red line) has an imposed anticyclonic wind speed maximum of 4.8 m/s, corresponding to a surface stress of $\tau_a = 0.04$ N/m^2, equivalent to the initial stress in the ice-driven scenario. Initially, the depth of the gyre (diagnosed by h) and its freshwater content increase linearly at a constant rate proportional to the vertical Ekman pumping of order $w_{\text{Ek}} \approx \tau_a/(\rho f R) \approx$ 30 m/year (Figure 2b, thick red line). The linear increase in h proceeds until baroclinic instability develops. By year 2 of the simulation, $h \approx 120$ m and the freshwater content anomaly reaches 40,000 km^3 or twice the asymptotic values of the ice-driven scenario despite the initial Ekman pumping rate being the same. Baroclinic instability ultimately arrests the deepening with eddy fluxes transporting freshwater laterally out of the gyre (Figure 2a, right). The gyre then reaches a quasi-steady equilibrium characterized by an active eddy field and a balance between Ekman downwelling and eddy fluxes. This is the limit case studied by Manucharyan et al. (2016), Manucharyan and Spall (2016), and Meneghello et al. (2017).

The statistically steady state equilibrium of the gyre can be described as a balance between the mean (Eulerian) overturning streamfunction (proportional to surface wind stress) and the eddy overturning streamfunction (Andrews & McIntyre, 1976; Doddridge et al., 2016; Marshall & Radko, 2003; Plumb & Ferrari, 2005). This vanishing residual mean circulation framework (Meneghello et al., 2017) yields the following scaling for the equilibrated value of h:

$$H_K \sim \frac{R}{\rho f K}\tau_a = \frac{R}{\rho f K}\rho_a C_{Da} u_a^2 = u_a R\sqrt{\frac{\rho_a C_{Da}}{\rho f \kappa}}, \tag{7}$$

where K is eddy diffusivity and the subscript K indicates eddy equilibrated. The final equality assumes a linear relationship between eddy diffusivity and isopycnal slope, $K = \kappa H_K/R$ (for some constant κ). The linear relationship between u_a and equilibrated isopycnal depth H_K implied by equation (7) is clear over the range of

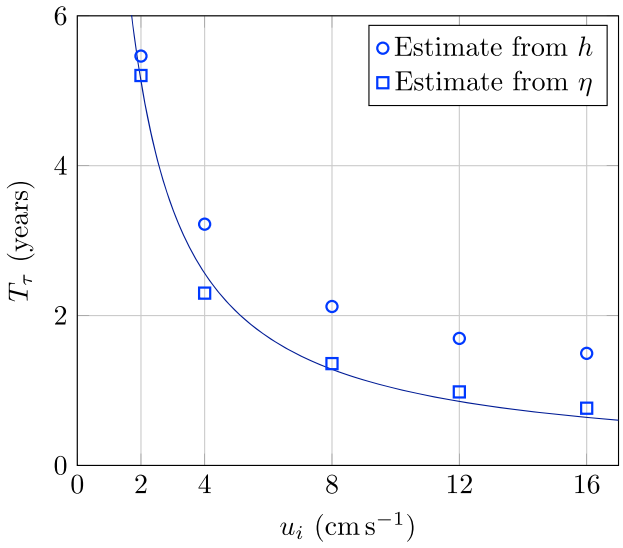

Figure 4. Equilibration time scale T_τ inferred by fitting (6) to the observed evolution of h (circles) and η (squares) for the ice-driven test cases. The blue line denotes the analytical solution from (5) with R = 300 km, $g' = 0.0063g$, $C_{Di} = 0.0055$, and $\gamma = 1.75$. The distance between the blue squares and blue circles quantifies the departure of the numerical model from our assumption of vanishing bottom pressure gradients, resulting in an underestimate of the surface velocity by (3).

imposed u_a in the five wind-driven simulations (Figure 3, red circles). Our results are in agreement with previous findings of Proshutinsky et al. (2002, 2009) and Davis et al. (2014) and the theory of Manucharyan et al. (2016), Manucharyan and Spall (2016), and Meneghello et al. (2017).

Finally, we carry out two experiments to examine the effect of a sudden transition between an ice-covered and an ice-free gyre. The eddying, deeper halocline transitions rapidly to a noneddying solution when the governor is turned on by adding the ice cover (Figure 2b, thin red line). The shallower, noneddying solution transitions to an eddying solution when the governor is turned off by removing the ice cover (Figure 2b, thin blue line).

3. Implications of the Ice-Ocean Stress Governor

We have analyzed and compared two different mechanisms governing the equilibration of the BG. In the wind-driven scenario in the absence of ice, the depth and freshwater content of the gyre is governed by the balance between Ekman pumping accumulating surface freshwater and a vigorous eddy field releasing it by baroclinic instability. This has been previously hypothesized to play a central role in gyre equilibration (Manucharyan & Spall, 2016; Manucharyan et al., 2016; Meneghello et al., 2017). Here we have described another fundamental mechanism, namely, the ice-ocean stress governor, a negative feedback between the ice-mediated Ekman pumping, and the surface geostrophic currents of the gyre. We have demonstrated how, in an ice-driven gyre, the spin-up of the gyre, its isopycnal depth anomaly, and its freshwater content can be regulated by the interaction between the sea ice and the surface geostrophic current flowing at comparable speeds. In this alternative scenario, the regulating mechanism drives the freshwater accumulation rate to zero rather than it being released by eddy transport.

We have considered both completely ice-covered ($\alpha = 1$) and ice-free ($\alpha = 0$) scenarios. It should be noted that in the presence of low ice concentrations, when ice is free drifting (i.e., no lateral internal ice stress), the ice is accelerated with respect to the geostrophic current until the air-ice stresses are in balance with the ice-ocean stresses. This is equivalent to the ice-free case. By contrast, internal stresses in a previously mobile ice would decouple the ice velocity from the wind, slow down the ice, and result in the anticyclonic gyre rubbing against the ice cover and spinning down, with upwelling and divergence of freshwater out of the gyre through surface Ekman processes. This is the case shown in our idealized setting by the thin red line in Figure 2b.

Here our focus has been the equilibrium state of the gyre, and our analysis is limited to time scales longer than the baroclinic adjustment time scale of the gyre; we assume that barotropic flows associated with the initial adjustment are damped and that (3) is appropriate.

How do an eddy equilibrated and a governor-equilibrated gyre compare? The simulations shown in Figure 2, which employ the same initial stress and Ekman pumping, suggest that the governor-equilibrated isopycnal depth anomaly (and accumulated freshwater) is about half of what one might expect if eddies were the balancing mechanism. While care must be taken when comparing the linear time scale of the eddy equilibration mechanism with the nonlinear time scale of the ice-ocean stress governor, the governor time scale is, depending on the assumed ice velocity, likely much faster than the eddy equilibration time scale $\frac{R^2}{K} \approx 10$ years.

Once at equilibrium, the wind-driven gyre can be disrupted in two ways, as summarized by the arrows in Figure 3: a change in the wind or ice speed, as suggested by previous authors (Giles et al., 2012), or a change in the effectiveness of the ice-ocean stress governor in reducing the surface stress, associated with a change in ice concentration. This suggests the potential for an important shift in BG dynamics under projected continued summer sea ice decline in the coming years and decades. Increased wind-driven Ekman downwelling in the summer and autumn on a gyre characterized by higher ice mobility (or no ice at all) will result in a deeper gyre and faster geostrophic currents. However, faster geostrophic currents will likely drive a strong upwelling during the ice-covered winters. One might expect a stronger seasonal cycle and spatial variability in isopycnal depth in a warmer Arctic. The effectiveness of the governor in reducing the surface stress will diminish as

the ice cover declines. Depending on the time scale of development of baroclinic instability, a more intense eddy field could develop during summer and autumn, to be subsequently damped by the ice cover during the following winter. This may in turn impact the dynamics of the halocline that insulates the ice cover from warmer waters at depth and hence the persistence of the ice cover itself.

Acknowledgments
The authors thankfully acknowledge support from NSF Polar Programs, both Arctic and Antarctic. NCEP Reanalysis data are provided by the NOAA/OAR/ESRL PSD, Boulder, Colorado, USA, from their Web site at `http://www.esrl.noaa.gov/psd/` (Kalnay et al., 1996). Arctic dynamic topography data were provided by the Centre for Polar Observation and Modelling, University College London `http://www.cpom.ucl.ac.uk/dynamic_topography` (Armitage et al., 2016). All data for this paper are properly cited and referred to in the reference list.

References

Andrews, D. G., & McIntyre, M. E. (1976). Planetary waves in horizontal and vertical shear: The generalized Eliassen-Palm relation and the mean zonal acceleration. *Journal of the Atmospheric Sciences*, *33*, 2031–2048. https://doi.org/10.1175/1520-0469(1976)033<2031:PWIHAV>2.0.CO;2

Armitage, T. W. K., Bacon, S., Ridout, A. L., Thomas, S. F., Aksenov, Y., & Wingham, D. J. (2016). Arctic sea surface height variability and change from satellite radar altimetry and GRACE, 2003–2014. *Journal of Geophysical Research: Oceans*, *121*, 4303–4322. https://doi.org/10.1002/2015JC011579

Bennet, S. (1993). *A history of control engineering, 1930–1955* (262 pp.). UK: IET. https://doi.org/10.1049/PBCE047E

Davis, P., Lique, C., & Johnson, H. L. (2014). On the link between Arctic sea ice decline and the freshwater content of the Beaufort Gyre: Insights from a simple process model. *Journal of Climate*, *27*(21), 8170–8184. https://doi.org/10.1175/JCLI-D-14-00090.1

Dewey, S., Morison, J., Kwok, R., Dickinson, S., Morison, D., & Andersen, R. (2018). Arctic ice-ocean coupling and gyre equilibration observed with remote sensing. *Geophysical Research Letters*, *45*, 1499–1508. https://doi.org/10.1002/2017GL076229

Doddridge, E. W., Marshall, D. P., & Hogg, A. M. (2016). Eddy cancellation of the Ekman cell in subtropical gyres. *Journal of Physical Oceanography*, *46*(10), 2995–3010. https://doi.org/10.1175/JPO-D-16-0097.1

Giles, K. A., Laxon, S. W., Ridout, A. L., Wingham, D. J., & Bacon, S. (2012). Western Arctic Ocean freshwater storage increased by wind-driven spin-up of the Beaufort Gyre. *Nature Geoscience*, *5*(3), 194–197. https://doi.org/10.1038/ngeo1379

Karsten, R., Jones, H., & Marshall, J. (2002). The role of eddy transfer in setting the stratification and transport of a circumpolar current. *Journal of Physical Oceanography*, *32*(1), 39–54. https://doi.org/10.1175/1520-0485(2002)032<0039:TROETI>2.0.CO;2

Kwok, R., & Morison, J. H. (2017). Recent changes in Arctic sea ice and ocean circulation. *US CLIVAR*, *15*(3), 1–6. https://doi.org/10.5065/D6833QQP

Lique, C., Johnson, H. L., & Davis, P. E. D. (2015). On the interplay between the circulation in the surface and the intermediate layers of the Arctic Ocean. *Journal of Physical Oceanography*, *45*(5), 1393–1409. https://doi.org/10.1175/JPO-D-14-0183.1

Manucharyan, G. E., & Spall, M. A. (2016). Wind-driven freshwater buildup and release in the Beaufort Gyre constrained by mesoscale eddies. *Geophysical Research Letters*, *43*, 273–282. https://doi.org/10.1002/2015GL065957

Manucharyan, G. E., Spall, M. A., & Thompson, A. F. (2016). A theory of the wind-driven Beaufort Gyre variability. *Journal of Physical Oceanography*, *2013*, 3263–3278. https://doi.org/10.1175/JPO-D-16-0091.1

Marshall, J., Adcroft, A., Hill, C., Perelman, L., & Heisey, C. (1997). A finite-volume, incompressible Navier Stokes model for studies of the ocean on parallel computers. *Journal of Geophysical Research*, *102*(C3), 5753–5766. https://doi.org/10.1029/96JC02775

Marshall, J., Hill, C., Perelman, L., & Adcroft, A. (1997). Hydrostatic, quasi-hydrostatic, and nonhydrostatic ocean modeling, *102*, 5733–5752. https://doi.org/10.1029/96JC02776

Marshall, J., & Radko, T. (2003). Residual-mean solutions for the Antarctic circumpolar current and its associated overturning circulation. *Journal of Physical Oceanography*, *33*(11), 2341–2354. https://doi.org/10.1175/1520-0485(2003)033<2341:RSFTAC>2.0.CO;2

Maxwell, J. C. (1867). On governors. *Proceedings of the Royal Society of London*, *16*, 270–283. https://doi.org/10.1098/rspl.1867.0055

McPhee, M. G., Proshutinsky, A., Morison, J. H., Steele, M., & Alkire, M. B. (2009). Rapid change in freshwater content of the Arctic Ocean. *Geophysical Research Letters*, *36*, L10602. https://doi.org/10.1029/2009GL037525

Meneghello, G., Marshall, J., Cole, S. T., & Timmermans, M.-L. (2017). Observational inferences of lateral eddy diffusivity in the halocline of the Beaufort Gyre. *Geophysical Research Letters*, *44*, 12,331–12,338. https://doi.org/10.1002/2017GL075126

Meneghello, G., Marshall, J., Timmermans, M.-L. L., & Scott, J. (2018). Observations of seasonal upwelling and downwelling in the Beaufort Sea mediated by sea ice. *Journal of Physical Oceanography*, *48*, 795–805. https://doi.org/10.1175/JPO-D-17-0188.1

Murray, J., Bradley, H., Craigie, W., Onions, C. T., Burchfield, R., Weiner, E., & Simpson, J. (2018). Governor, *The Oxford English dictionary* (Vol. VI, p. 713). Oxford: Clarendon Press; New York: Oxford University Press.

Nurser, A. J. G., & Bacon, S. (2014). The Rossby radius in the Arctic Ocean. *Ocean Science*, *10*(6), 967–975. https://doi.org/10.5194/os-10-967-2014

Plumb, R. A., & Ferrari, R. (2005). Transformed Eulerian-mean theory. Part I: Nonquasigeostrophic theory for eddies on a zonal-mean flow. *Journal of Physical Oceanography*, *35*(2), 165–174. https://doi.org/10.1175/JPO-2669.1

Proshutinsky, A., Bourke, R. H., & McLaughlin, F. A. (2002). The role of the Beaufort Gyre in Arctic climate variability: Seasonal to decadal climate scales. *Geophysical Research Letters*, *29*(23), 2100. https://doi.org/10.1029/2002GL015847

Proshutinsky, A., Dukhovskoy, D., Timmermans, M.-l., Krishfield, R., & Bamber, J. L. (2015). Arctic circulation regimes. *Philosophical Transactions. Series A, Mathematical, Physical, and Engineering Sciences*, *373*(2052), 20140160. https://doi.org/10.1098/rsta.2014.0160

Proshutinsky, A. Y., & Johnson, M. A. (1997). Two circulation regimes of the wind-driven Arctic Ocean. *Journal of Geophysical Research*, *102*(C6), 12,493–12,514. https://doi.org/10.1029/97JC00738

Proshutinsky, A., Krishfield, R., Timmermans, M.-L., Toole, J., Carmack, E., Mclaughlin, F., et al. (2009). Beaufort Gyre freshwater reservoir: State and variability from observations. *Journal of Geophysical Research*, *114*, 1–25. https://doi.org/10.1029/2008JC005104

Timmermans, M. L., Proshutinsky, A., Krishfield, R. A., Perovich, D. K., Richter-Menge, J. A., Stanton, T. P., & Toole, J. M. (2011). Surface freshening in the Arctic Ocean's Eurasian Basin: An apparent consequence of recent change in the wind-driven circulation. *Journal of Geophysical Research*, *116*, C00D03. https://doi.org/10.1029/2011JC006975

Yang, J. (2006). The seasonal variability of the Arctic Ocean Ekman transport and its role in the mixed layer heat and salt fluxes. *Journal of Climate*, *19*(20), 5366–5387. https://doi.org/10.1175/JCLI3892.1

Yang, J. (2009). Seasonal and interannual variability of downwelling in the Beaufort Sea. *Journal of Geophysical Research*, *114*, C00A14. https://doi.org/10.1029/2008JC005084

Yang, J., Proshutinsky, A., & Lin, X. (2016). Dynamics of an idealized Beaufort Gyre: 1. The effect of a small beta and lack of western boundaries. *Journal of Geophysical Research: Oceans*, *121*, 1249–1261. https://doi.org/10.1002/2015JC011296

Zhang, J., Steele, M., Runciman, K., Dewey, S., Morison, J., Lee, C., et al. (2016). The Beaufort Gyre intensification and stabilization: A model-observation synthesis. *Journal of Geophysical Research: Oceans*, *121*, 7933–7952. https://doi.org/10.1002/2016JC012196

Zhong, W., Steele, M., Zhang, J., & Zhao, J. (2018). Greater role of geostrophic currents in Ekman dynamics in the western Arctic Ocean as a mechanism for Beaufort Gyre stabilization. *Journal of Geophysical Research: Oceans*, *123*, 149–165. https://doi.org/10.1002/2017JC013282